COSMOLOGICAL FORMATION OF LOW-MASS OBJECTS

ZOLTÁN HAIMAN,[1,3] ANNE A. THOUL,[2] AND ABRAHAM LOEB[1,2]

ABSTRACT

We investigate the early formation of bound objects with masses comparable to the cosmological Jeans mass ($\sim 10^5 \, M_\odot$). We follow the growth of isolated spherically symmetric density peaks starting from the linear perturbative regime. The initial parameters correspond to density peaks of various widths and heights in a cold dark matter cosmology. We use a one-dimensional spherical Lagrangian hydrodynamics code to follow the dynamical, thermal, and nonequilibrium chemical evolution of the gas. The system includes a collisionless dark matter component and a baryonic component composed of the nine species H, H^-, H^+, He, He^+, He^{++}, H_2, H_2^+, and e^-. All relevant chemical reactions between these species and their cooling mechanisms are included in the calculations.

We explore the dependence of the dynamical evolution of the gas on two parameters: the initial mass scale and the initial overdensity of the system. We follow the evolution of the density, temperature, and abundance profiles within the cloud, assuming two types of central boundary conditions for the collisionless component: in one the infalling dark matter virializes through a reflection from a hard sphere, while in the other it accretes onto a central sink. We find that in both cases, radiative cooling by H_2 affects the collapse dynamics of the gas only after it has already virialized and become part of the bound object. Therefore, radiative cooling is unlikely to have triggered the initial collapse of perturbations at redshifts $z > 10$. Nevertheless, baryonic objects with masses well below the linear theory Jeans mass ($\lesssim 10^3 \, M_\odot$) form at high redshifts because of shell crossing by the dark matter. Such objects could be the progenitors of a primordial population of high-mass stars in the intergalactic medium.

Subject headings: cosmology: theory — early universe — galaxies: formation — hydrodynamics

1. INTRODUCTION

Observations indicate that by a redshift ~ 5 the universe contained nonlinear objects such as quasars and absorption systems (see, e.g., Frenk et al. 1989). As current quasar searches are limited from probing even higher redshifts by observational limitations, there is no reason to suspect that they have already revealed the first generation of baryonic objects in the universe. In fact, popular cold dark matter (CDM) cosmologies predict the collapse of the first baryonic objects as early as $z \sim 30$ on a mass scale just above the cosmological Jeans mass $\sim 10^5 \, M_\odot$ (Peebles 1993).

The earliest baryonic objects are interesting for a variety of reasons. First, in the bottom-up hierarchical picture of structure formation, they provide the elementary building blocks for larger mass objects that form later (see, e.g., Blumenthal et al. 1984). For example, Peebles & Dicke (1968) have suggested that globular clusters may be the fossils of Jeans mass objects that collapsed and fragmented into stars at high redshifts, long before galactic halos formed. Second, direct detection of low-mass objects at $z \gtrsim 10$ can be used to place constraints on the power spectrum of primordial density fluctuations on very small scales that cannot be probed by microwave background anisotropy experiments (e.g., White, Scott, & Silk 1994). Third, the first baryonic objects may have fragmented into stars and contaminated the intergalactic medium with metals through supernova-driven winds. Recent spectroscopic observations with the Keck telescope indicate the existence of a nonzero metallicity even in Lyα clouds (Fan 1994; Tytler & Fan 1995).

The evolution of the first baryonic objects depends on their molecular composition and thermodynamic state. The chemistry and radiative cooling during the cosmological collapse of these objects define a well-posed problem for investigation, since the element abundances are fixed by primordial nucleosynthesis and the cooling rates are not complicated (at least initially) by energy input or metal enrichment from stars or quasars. This situation is changed during the later evolutionary stages of these clouds, because of both internal and external ionizing sources or supernovae. We will address this feedback in a forthcoming publication (Haiman & Loeb 1996).

Under primordial conditions, molecular hydrogen (H_2) could become the most efficient coolant of collapsing clouds. Indeed, it has been suggested by various authors (e.g., Saslaw & Zipoy 1967; Peebles & Dicke 1968; Hirasawa 1969; Matsuda, Sato, & Takeda 1969; Hutchins 1976; and more recently, Silk 1983; Palla, Salpeter, & Stahler 1983; Lepp & Shull 1984; Couchman 1985; Lahav 1986) that radiative H_2 cooling may, in fact, control the formation of the first generation of objects. However, these suggestions were based on highly simplified models involving homogeneous clouds that cool radiatively while undergoing a uniform free-fall collapse. In reality, a collapsing system becomes highly inhomogeneous as its central density increases. The resulting density profile tends to steepen until a shock develops (see, e.g., Bertschinger 1985 for self-similar solutions well above the Jeans mass). As the shock thermalizes the kinetic energy of the infalling gas, it alters considerably the thermal history of the gas relative to the predictions of the homogeneous collapse models.

In order to study the effect of molecular cooling on collapsing primordial clouds, it is necessary to follow both the dynamics of the gas as a whole and the chemical evolution of its various molecular components. It has only recently

[1] Astronomy Department, Harvard University, 60 Garden Street, Cambridge, MA 02138.
[2] Institute for Advanced Study, Olden Lane, Princeton, NJ 08540.
[3] Institute of Astronomy, Cambridge University, Madingley Road, Cambridge CB3 1RZ, UK.

become computationally possible to incorporate gas-dynamics into three-dimensional numerical simulations (Cen & Ostriker 1994; Evrard, Summers, & Davis 1994; Navarro & White 1994; Steinmetz & Muller 1994; Shapiro, Giroux, & Babul 1994; Hernquist, Katz, & Weinberg 1995; Quinn, Katz, & Efstathiou 1995). Unfortunately, these three-dimensional hydrodynamic simulations still suffer from limited spatial and mass resolution. Furthermore, they usually focus on the formation of galaxy-size objects. Here we use a one-dimensional Lagrangian code (Thoul & Weinberg 1995) to examine the evolution of spherically symmetric systems at high redshifts. We follow in detail the dynamical, thermal, and chemical evolution of a spherical system made of collisionless dark matter and collisional gas. While the geometry is idealized, this one-dimensional simulation can achieve much higher spatial and mass resolution than three-dimensional simulations, computing gasdynamic processes with higher accuracy. Because one can easily visualize the results from one-dimensional simulations, it is often straightforward to interpret the underlying physics in these runs. But most importantly, since these simulations are inexpensive, it is possible to explore a larger range of parameter space with them.

The minimum baryonic mass of the first generation of objects is defined by the smallest scale over which the repulsive pressure force is unable to counteract the attractive gravitational force. Since molecular hydrogen formation becomes more effective as the gas density increases, H_2 cooling can provide a positive feedback that reduces the gas pressure as the density increases, thus allowing the density to increase even further. In this paper we address the question: *could molecular cooling lower the mass of the first baryonic objects down to low (possibly stellar) values?*

The outline of the paper is as follows. In § 2 we review the notion of a cosmological Jeans mass based on linear perturbation theory and describe how the presence of dark matter, nonlinearities, or cooling affect this notion. In § 3 we describe the numerical code and its ability to reproduce various analytical results. In § 4 we present numerical results for the evolution of clouds with different initial conditions. In particular, we identify the regime of mass scales and density contrasts over which radiative cooling by H_2 affects the collapse dynamics. Finally, § 5 summarizes the implications of these results for the first generation of bound objects in the universe.

2. SPHERICAL COLLAPSE AND THE COSMOLOGICAL JEANS MASS

The Jeans length λ_J was originally defined (Jeans 1928) in Newtonian gravity as the critical wavelength that separates oscillatory and exponentially growing sinusoidal density perturbations in an infinite, uniform, and stationary distribution of gas. On scales smaller than λ_J, the sound-crossing time is shorter than the gravitational free-fall time, allowing the build-up of a pressure force to balance gravity. The Jeans mass is defined as the mass within a sphere of radius $\lambda_J/2$, $M_J = (4\pi/3)\rho(\lambda_J/2)^3$. In a perturbation with a mass greater than M_J, self-gravity cannot be supported by pressure, and so the gas is unstable to gravitational collapse. The Newtonian derivation of the Jeans instability suffers from conceptual inconsistency, as the unperturbed gravitational force of the uniform background must induce bulk motions (see Binney & Tremaine 1987). However, this inconsistency is remedied when the analysis is done in an expanding universe.

The perturbative derivation of the Jeans instability criterion can be carried out in a cosmological setting by considering a sinusoidal perturbation superposed on a uniformly expanding background. Here, as in the Newtonian limit, there is a critical wavelength λ_J that separates oscillatory and growing modes. Although the expansion of the background slows down the exponential growth of the amplitude to a power-law growth, the fundamental concept of a minimum mass that can collapse at any given time remains the same (see, e.g., Kolb & Turner 1990; Peebles 1993).

To be specific, let us consider an Einstein–de Sitter universe with $\Omega_{dm} + \Omega_b = 1$, where $\Omega_{dm} = \bar{\rho}_{dm}/\rho_c$, $\Omega_b = \bar{\rho}_b/\rho_c$, $\bar{\rho}_{dm}$ is the average dark matter density, $\bar{\rho}_b$ is the average baryonic density, and ρ_c is the critical density. We assume spatial fluctuations in the gas and dark matter densities in the form of a single spherical Fourier mode,

$$\frac{\rho_{dm}(r, t) - \bar{\rho}_{dm}(t)}{\bar{\rho}_{dm}(t)} = \delta_{dm}(t) \frac{\sin (kr)}{kr} \qquad (1)$$

$$\frac{\rho_b(r, t) - \bar{\rho}_b(t)}{\bar{\rho}_b(t)} = \delta_b(t) \frac{\sin (kr)}{kr}, \qquad (2)$$

where $\bar{\rho}_{dm}(t)$ and $\bar{\rho}_b(t)$ are the background densities of the dark matter and baryons, $\delta_{dm}(t)$ and $\delta_b(t)$ are the dark matter and baryon overdensity amplitudes, r is the comoving radial coordinate, and k is the comoving perturbation wavenumber. We assume a $\gamma = 5/3$ ideal gas equation of state for the baryons. Initially, at time $t = t_i$, the gas temperature is uniform $T_b(r, t_i) = T_i$, and the perturbation amplitudes are small $\delta_{dm,i}$, $\delta_{b,i} \ll 1$. We define the region inside the first zero of $\sin (kr)/(kr)$, namely, $0 < kr < \pi$, as the "cloud."

The evolution of $T_b(r, t)$ is determined by the coupling of free electrons to the cosmic background radiation (CBR) through Compton scattering, by the adiabatic expansion of the gas, and by other radiative heating and cooling processes. Depending on the detailed chemical composition of the baryons, $T_b(r, t)$ will be somewhere between the CBR temperature $T_\gamma \propto t^{-2/3}$ and the adiabatically scaled temperature $T_{ad} \propto t^{-4/3}$. In the limit of tight coupling to T_γ, the gas temperature remains uniform. On the other hand, in the adiabatic limit, the temperature develops a gradient according to the relation

$$T_b \propto \rho_b^{(\gamma - 1)}. \qquad (3)$$

The evolution of $\delta_{dm}(t)$ in the linear regime is described by the equation

$$\left(\frac{d^2}{dt^2} + \frac{4}{3t} \frac{d}{dt}\right)\delta_{dm} = \frac{2}{3t^2}(\Omega_b \delta_b + \Omega_{dm} \delta_{dm}) \qquad (4)$$

(Kolb & Turner 1990), whereas the evolution of $\delta_b(t)$ is described by

$$\left(\frac{d^2}{dt^2} + \frac{4}{3t} \frac{d}{dt}\right)\delta_b = \frac{2}{3t^2}(\Omega_b \delta_b + \Omega_{dm} \delta_{dm})$$
$$- \frac{k_B T_i}{\mu m_p} k^2 \left(\frac{t_0}{t}\right)^{4/3}\left(\frac{t_i}{t}\right)^{(2+2\beta)/3}\left[\delta_b + \frac{2}{3}\beta(\delta_b - \delta_{b,i})\right]. \qquad (5)$$

Here m_p is the proton mass, μ is the mean molecular weight of the gas, k_B is Boltzmann's constant, and t_0 is the present age of the universe. The parameter β distinguishes between

the two limits for the evolution of the gas temperature. In the adiabatic limit $\beta = 1$, and when the baryon temperature is uniform and locked to the background radiation, $\beta = 0$. The last term on the right-hand side (inside the inner parentheses) takes into account the extra pressure gradient force in $\nabla(\rho_b T) = (T\nabla\rho_b + \rho_b\nabla T)$, arising from the temperature gradient that develops according to equation (3) in the adiabatic limit. The Jeans wavelength $\lambda_J = 2\pi/k_J$ is obtained by setting the right-hand side of equation (5) to zero and solving for the critical wavenumber k_J. As can be seen from equation (5), the critical wavelength λ_J (and therefore the mass M_J) is time dependent.[4] We infer from equation (5) that as time proceeds, perturbations with increasingly smaller initial wavelengths stop oscillating and start to grow. To derive the time evolution of λ_J, we must solve for the time evolution of the temperature $T_b(r, t)$, including the effects of the various cooling and heating mechanisms, and the evolution of the chemical composition of the baryons.

Another, more fundamental, difficulty is to relate the Jeans mass to the mass of collapsed, bound objects. The above analysis is perturbative (eqs. [4] and [5] are valid only while δ_b, $\delta_{dm} \lesssim 1$) and can only describe the initial phase of the collapse. As δ_b and δ_{dm} grow and become larger than unity, the density profiles start to evolve. In particular, since material at various radii collapses at different times, there is no reason to assume that the collapsed object includes the entire mass within the original density peak. Indeed, it has been realized (Larson 1969) that in the nonlinear regime the density and temperature profiles steepen considerably and the central part of the sphere becomes exceedingly dense and hot. An object may form in the center and subsequently accrete material from the original peak. In the limit of high masses ($\lambda \gg \lambda_J$) and in the absence of radiative cooling, the gas particles virialize through a shock that propagates outward from the center of the sphere. The shock structure and the evolution of the density profile is self-similar, and near the center the density approaches the power-law profile $\rho \propto r^{-2.25}$ (this was first predicted by Gott 1975, and later proved via a semianalytic approach by Bertschinger 1985). Although the initial perturbation has a definite mass, it is not clear what mass to associate with the end-product of the collapse. The relation between the mass of the bound object M_{obj} and the parameters of the initial perturbation can be expressed as $M_{obj} = M_{obj}(k, \delta_{dm,i}, \delta_{b,i}, t_i, t)$. This relation cannot be inferred directly from linear theory.

In the presence of radiative cooling, the dynamical evolution of the gas departs from self-similarity. In the limit of very efficient cooling, gas particles follow free-fall trajectories until they come arbitrarily close to the origin. If the cooling time is comparable to the dynamical time, the gas particles go through various phases of partial pressure support (see, e.g., Thoul & Weinberg 1995). In general, radiative cooling will facilitate the collapse of the clouds, since it reduces the pressure support of the gas. Thus we expect that $M_{obj}(k, \delta_{dm,i}, \delta_{b,i}, t_i, t)$ will be increased relative to its value in the absence of cooling.

[4] In the limit $\Omega_b \ll \Omega_{dm} \approx 1$ and $T_b \approx T_\gamma$ (i.e., $\beta = 0$ in eq. [5]), the growing solution to equation (4) gives $\delta_{dm} \propto t^{-2/3}$, and equation (5) can be made homogeneous in time. In this limit, i.e., when almost all the mass is in dark matter and the density of free electrons is sufficiently high to lock the gas temperature to the CBR temperature, λ_J becomes approximately time independent.

The Jeans mass derived from linear theory specifies whether an initial perturbation, characterized by the parameters k, $\delta_{dm,i}$, $\delta_{b,i}$, and t_i, starts to grow. To determine the mass of the bound object resulting from its collapse, we must follow numerically the nonlinear evolution of the density peak, including all microphysical gas processes. In the following sections, we address this problem using a one-dimensional spherically symmetric hydrodynamical code.

3. THE NUMERICAL CODE

3.1. *Description of the Code*

The code we use is a modified version of the one-dimensional, spherically symmetric Lagrangian hydrodynamics code written by Thoul (Thoul & Weinberg 1995). The code evolves a mixture of two fluids by moving concentric spherical shells of fixed mass in the radial direction. For the column densities of interest here, the gas is assumed to be optically thin. A description of the numerical method and the details of the original code can be found in the above reference. Here we only summarize the equations solved by the code and describe briefly the new additions: chemical reactions, Compton cooling, and cooling by the H_2 molecule.

The Lagrangian equations of hydrodynamics in spherical symmetry are the continuity equation for the baryons,

$$\frac{dm_b}{dr_b} = 4\pi r_b^2 \rho_b , \tag{6}$$

the momentum equations for the baryons and dark matter,

$$\frac{dv_b}{dt} = -4\pi r_b^2 \frac{dp}{dm_b} - \frac{M(r_b)}{r_b^2} , \tag{7}$$

$$\frac{dv_{dm}}{dt} = -\frac{M(r_{dm})}{r_{dm}^2} , \tag{8}$$

the energy equation,

$$\frac{du}{dt} = -p \frac{d(\rho_b^{-1})}{dt} + \frac{\Lambda}{\rho_b} , \tag{9}$$

and the equation of state,

$$p = (\gamma - 1)\rho_b u . \tag{10}$$

Here $\gamma = 5/3$ is the adiabatic index, and we have set $G = 1$. Each baryonic shell is described by its radius r_b, velocity v_b, mass density ρ_b, pressure p, internal energy per unit mass u, and the baryonic mass interior to it m_b. The dark matter shells are described by their radius r_{dm}, velocity v_{dm}, and the enclosed dark matter mass m_{dm}. $M(r)$ is the total (baryonic plus dark matter) mass inside a shell at radius r. The details of the cooling terms included in Λ in equation (9) are given in Appendix A.

The baryonic component is composed of the nine species H, H^-, H^+, He, He^+, He^{++}, H_2, H_2^+, and e^-. For the ith species, we denote the total number of particles by N_i, the number density and molecular weight of these particles by n_i and μ_i, respectively, and the mass fraction by

$$y_i = \frac{\mu_i n_i}{\sum_{j=1}^9 \mu_j n_j} = \frac{\mu_i n_i}{\rho_b} . \tag{11}$$

The relative abundances of helium species ($i = 4, 5, 6$) are denoted by $x_i = n_i/n_{He,tot}$, and the relative abundance of the

hydrogen species ($i = 1, 2, 3, 7, 8$) and electrons ($i = 9$) are given by $x_i = n_i/n_{\rm H, tot}$, where $n_{\rm He, tot} \equiv (n_{\rm He} + n_{\rm He+} + n_{\rm He++})$ and $n_{\rm H, tot} \equiv (n_{\rm H} + n_{\rm H+} + n_{\rm H-} + 2n_{\rm H_2} + 2n_{\rm H_2+})$.

The above nine species interact through various chemical reactions. Only the global quantity ρ_b appears in the hydrodynamical equations (6)–(10). After each shell has been moved to its new location by a hydrodynamical iteration, the nine species are allowed to interact for a time $dt_{\rm H}$, and the relative abundances in each shell are upgraded according to the rate equations

$$\frac{dn_i}{dt} = \sum_{l=1}^{9} \sum_{m=1}^{9} a_{lmi} k_{lm} n_l n_m + \sum_{j=1}^{9} b_{ji} k_j n_j . \quad (12)$$

Here the k_{lm} denote reaction rate coefficients, k_n represent photoionization or photodissociation integrals, and a_{lmi}, $b_{ni} = 0, \pm 1$, or ± 2, depending on the reaction. The next hydrodynamical iteration starts at a time interval $dt_{\rm H}$ later, with the updated relative abundances. In Appendix B we provide a table of the chemical reactions, and the adopted rate coefficients and cross sections.

A complication to the above numerical approach arises because of the stiffness of the system of differential equations (12). The stiffness increases the required computation time by a large factor, because standard solver routines for differential equations require exceedingly small time steps, while routines designed to solve a stiff system of equations require many matrix operations with 9×9 matrices, in our case. We have experimented with each routine in Numerical Recipes (Press et al. 1992) and have found the routine STIFBS to be the most efficient. We also compared the performance of STIFBS with the more popular routine LSODAR (Hindmarsh 1983) to solve the system of equations (12). We found STIFBS to produce identical answers $\sim 20\%$ faster than LSODAR. The nine equations in system of equations (12) could be reduced to six, using the conservation equations for the hydrogen and helium mass and for the charge. However, we found that this reduction actually *increases* the computation time, because the use of the algebraic conservation laws requires that the calculation of each number density n_i be done to a much higher degree of accuracy than otherwise necessary. Another simplification could arise if the species were either "frozen" or reached equilibrium within a hydrodynamical iteration time. Unfortunately, equations (12) do not have a single time constant, and the concentrations of different species change on different timescales; in particular, $n_{\rm H_2}$ evolves on the hydrodynamic timescale. The only simplification we were able to make was to freeze the helium abundances during the initial phase of the dynamical evolution, thus reducing the number of equations to be solved from nine to six.

We adopt two different central boundary conditions, corresponding to placing either a hard sphere or a sink (black hole) in the center (see Thoul & Weinberg 1995). In the first case, the dark matter virializes by bouncing off the hard sphere, while in the latter case the dark matter falls freely into a central sink. The first case may provide a more realistic representation of collapsing regions in the universe, for which nonspherical motions (or angular momentum) define an inner boundary to the infall. Quantities for the nth shell are always calculated using information from the nth and $(n + 1)$th shells; thus boundary effects from the surface of the sphere propagate inward by one shell at each iteration. In order to avoid unphysical contamination of the results

by signals propagating from the outermost shell in the simulation, we choose the outer boundary condition to be such that the total perturbed mass inside the outermost shell is zero, *and* the density profile has zero slope at the surface. Both of these conditions are satisfied at the first minimum of the $\sin (x)/x$ function in equations (1) and (2), i.e., at $x = 4.4934$. This choice eliminates both pressure and gravitational forces on the outermost shell and allows this shell to simply follow the general expansion of the universe.

3.2. *Tests of the Code*

Although Thoul & Weinberg (1995) have made extensive tests of the code, we performed a few additional tests. The most important side effect of the addition of the chemical rate equations was an increase in computation time by approximately a factor of 10. This forced us to use a lower resolution (500 gas shells and 5000 dark matter shells) in our runs. However, comparisons with runs of 5 times higher resolution (2500 gas shells, 25,000 dark matter shells) showed no considerable differences in the trajectories of the shells.

The numerical code contains three almost independent modules. These modules perform the hydrodynamical, chemical, and cooling calculations. We tested these three modules as follows.

1. *Hydrodynamics.*—The hydrodynamics part of the code was tested by Thoul & Weinberg (1995). They reproduced analytical solutions for pulsations of a polytrope and for the self-similar collapse of a spherically symmetric, cosmological perturbation (Bertschinger 1985). In order to test the code in a context closer to the present application, we checked that it reproduces the evolution of the density contrast in the linear regime. The linear theory for the evolution of the density contrast of a single spherical Fourier mode was described in § 2 above. Supplemented with the temperature evolution $T_b(t)$, this calculation yields the factor $\delta_k(t)$ in

$$\delta(r, t) \equiv \frac{\delta \rho}{\rho} (r, t) = \delta_k(t) \frac{\sin (kr)}{kr} \quad (13)$$

for each value of k for both the dark matter and the gas. We ran the code with an initial overdensity profile given in equations (1) and (2) for various values of k and $\delta_k(t = 0) = 0.05$. We found that the shape of the profile stays unchanged to a high precision, while the overdensity changes by an overall factor very close to the value predicted from linear theory. Figure 1 shows how closely the overdensity in three gas shells follow the predicted $\delta_k(t)$, for four different values of k.

2. *Chemistry.*—To test the numerical integrations of the system of chemical reaction equations (12), we checked that the total hydrogen and helium mass and the total charge are conserved, or equivalently that the quantities

$$N_{\rm H, tot} = N_{\rm H} + N_{\rm H+} + N_{\rm H-} + 2N_{\rm H_2} + 2N_{\rm H_2+} , \quad (14)$$

$$N_{\rm He, tot} = N_{\rm He} + N_{\rm He+} + N_{\rm He++} , \quad (15)$$

and

$$Q_{\rm tot} = N_{\rm H+} - N_{\rm H-} + N_{\rm He+} + 2N_{\rm He++} + N_{\rm H_2+} - N_e \quad (16)$$

are constant in time in each shell. We found all three quantities to be conserved to at least one part in 10^8. We also checked that the abundances converge to the correct equi-
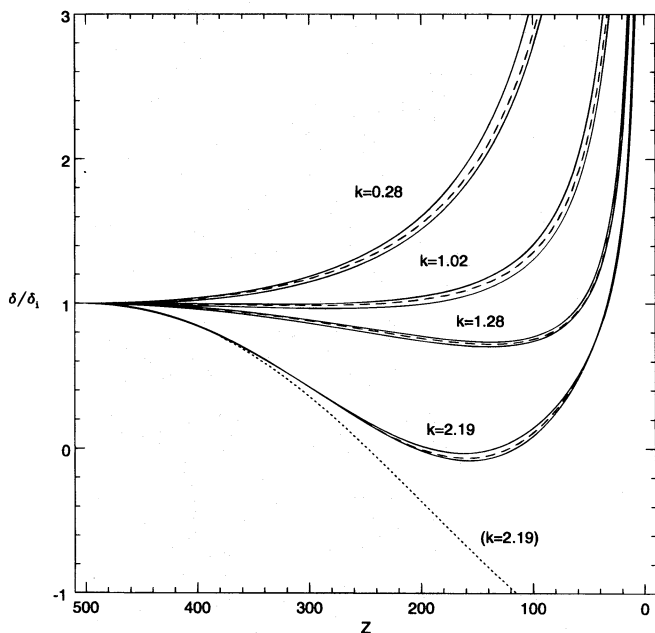
Fig. 1.—Evolution of the overdensity for single spherical Fourier modes in the linear regime. The overdensity δ is normalized to its initial value δ_i. The comoving wavenumber k is given in kpc^{-1}. The dashed lines are obtained analytically from linear theory. The pairs of solid lines show numerical results for $\delta(r, z)$ at the center and at the surface of the sphere. The overdensity at the center of the sphere becomes slightly higher than at the surface. The dotted line shows the analytic results from linear theory when the temperature gradient term in the square brackets in equation (5) of § 2 is ignored.

librium values. We ran the routine STIFBS starting with the set of initial concentrations $x_{H_2} = 1.7 \times 10^{-6}$, $y_{He} = 0.24$, and $y_H \approx 0.76$ at various temperatures, until none of the abundances changed by more than 0.1% from one step to the next. Since the abundances of H_2, H^-, and H_2^+ are always very small, by eliminating these three species from the system of equations (12), and by setting $d/dt = 0$, one can find algebraically the expected equilibrium abundances of the six remaining species. We found that STIFBS indeed converged to these values. Figure 2 shows the equilibrium abundances of all nine species versus temperature.

3. *Cooling and chemistry.*—Several authors have considered molecular cooling of a uniform sphere in free-fall collapse (e.g., Palla et al. 1983; Lepp & Shull 1984). The general conclusion from these studies can be summarized as follows. On a temperature versus density plot, the temperature departs from the adiabatic relation, $T_b \propto \rho_b^{2/3}$, because of H_2 cooling and achieves a local maximum T_{max}, after which it turns around and declines as the density increases further. The temperature does not start to rise again over several decades of increase in density. The exact values of T_{max}, the density at the turnaround in temperature, and the density at which the temperature starts to rise again all depend on the adopted reaction rates and cooling function, as well as on the initial size, density temperature, and composition of the sphere.

We therefore tested only the general conclusion that a turnaround in temperature should occur and that the temperature should not increase over the next several decades in density. We considered a uniform sphere in a homogeneous free-fall collapse with the following initial parameters: $R = 10^{21}$ cm, $\rho_0 = 4.52 \times 10^{-26}$ g cm^{-3}, $T = 64$ K,

$x_{H_2} = 1.7 \times 10^{-6}$, $y_{He} = 0.24$, and $y_H \approx 0.76$. The chemical reactions and cooling mechanisms are summarized in Appendices A and B. The resulting temperature versus density plot as well as the relative abundance of H_2 versus density are shown in Figure 3. As seen in this figure, turnaround indeed occurs at $\rho/\rho_0 = 80$ when the temperature reaches the maximum value $T_{max} \sim 400$ K. We note that the relative abundance of H_2 reaches $x_{H_2} = 3.8 \times 10^{-3}$, which is consistent with the H_2 fractions in Palla et al. (1983) and Lepp & Shull (1984).

4. NUMERICAL RESULTS AND DISCUSSION

4.1. *Initial Conditions*

For all cases presented in this paper, we adopt a Hubble constant of $H_0 = 50$ km s^{-1} Mpc^{-1} ($h = 0.5$). In runs with dark matter, we assume an Einstein–de Sitter universe with $\Omega_{dm} = 0.9$, $\Omega_b = 0.1$, and in runs without dark matter, we assume an open universe with $\Omega_b = 0.1$. We start the integrations at $z_i = 500$, when the perturbations are still in the linear regime. The temperature for the CBR is taken to be $T_\gamma = 2.726(1 + z)$ K (Mather et al. 1994), and the initial temperature of the cloud is assumed to be uniform and equal to T_γ at z_i. We use spherical k-modes as the initial overdensity profiles,

$$\rho_{dm,i}(r) = \Omega_{dm} \rho_c \left[1 + \delta_{dm,i} \frac{\sin(kr)}{kr} \right], \qquad (17)$$

$$\rho_{b,i}(r) = \Omega_b \rho_c \left[1 + \delta_{b,i} \frac{\sin(kr)}{kr} \right], \qquad (18)$$

where $\rho_c = (6\pi G t^2)^{-1}$ is the critical density. With this choice, the evolution in the linear regime can be compared directly to the prediction of equations (4) and (5). As mentioned at the end of § 3.1, this choice also eliminates numerical edge effects at the outer boundary. We have experimented with alternative overdensity profiles, such as a Gaussian, or the most probable profile for random Gaussian fluctuations (Bardeen et al. 1986, hereafter BBKS), and found that our qualitative conclusions are insensitive to the detailed shape of the initial density profile.

The density profiles in equations (17) and (18) can be used to define three characteristic mass scales. First, the total baryonic mass that is gravitationally bound includes all the baryonic material enclosed by the radius corresponding to the first *minimum* of $\sin(kr)/(kr)$, i.e., inside $kR_{bound} = 4.4934$. We denote this mass as M_{bound}. Second, we define the mass of the baryonic material that has a positive overdensity [i.e., contained within the first *zero* of $\sin(kr)/(kr)$, at $kR_{cloud} = \pi$] to be M_{cloud}. Finally, the baryonic mass that has virialized and condensed into a central object, M_{obj}, is redshift dependent and will be defined more precisely in the next section.

The initial amplitude of the dark matter density profile perturbation can be written as $\delta_{dm,i} = \nu\sigma$, where σ is the rms density fluctuation within some filter of a given shape and size in the CDM model. The value of ν characterizes the likelihood of the occurrence of the peak in a Gaussian density field. This characterization depends weakly on the shape and size of the filter, and strongly on the choice of power spectrum. For reference, we quote in Table 1 the value of σ for six different mass scales, M_{cloud}, and two different filter shapes with the *COBE*-normalized BBKS power spectrum. The values in this table were obtained under the normalization $\sigma_{8h^{-1}Mpc} = 1.22$ (for $\Omega_{dm} = 0.9$ and
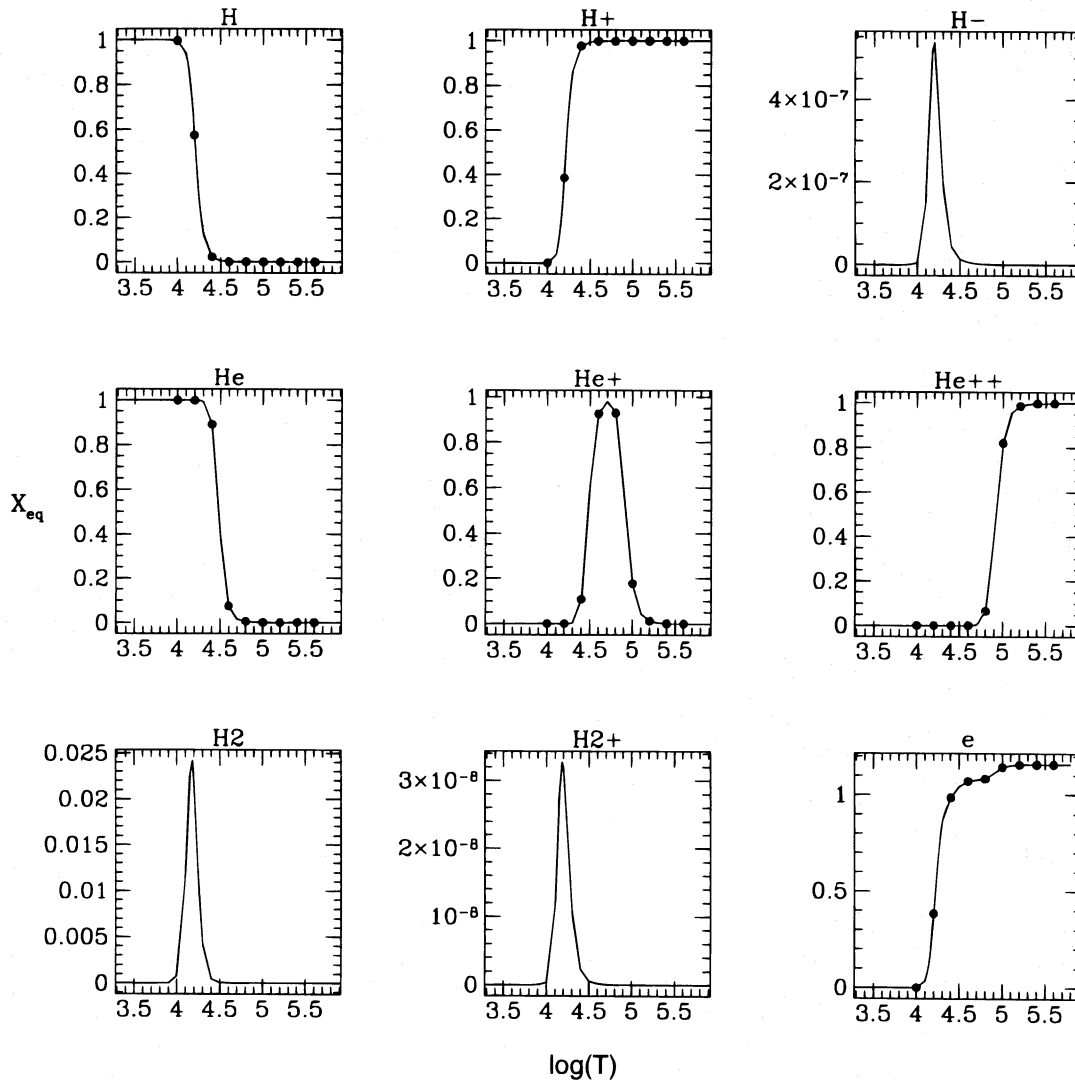
Fig. 2.—Equilibrium abundances of the nine species as a function of temperature. The abundances were obtained by integrating equations (12) with the routine STIFBS until the abundances reached their equilibrium values. The dots show values obtained algebraically from equations (12) by setting $n_{H_2} = n_{H^-} = n_{H_2^+} = 0$ and $d/dt = 0$.

$h = 0.5$; see Bunn, Scott, & White 1995), using a filter radius $R_f = 0.12 R_{cloud}$. The initial amplitude of the baryon density perturbation is a small fraction of the dark matter amplitude, because the baryons had been locked to the CBR until $z \approx 10^3$, while the dark matter fluctuations have had more time to grow since matter-radiation equality. We chose the

somewhat arbitrary value $\delta_{b,i} = (1/10)\delta_{dm,i}$ to take this effect into account; our results are insensitive to the precise value of this ratio. Because of the tight coupling of the baryons to the CBR before the recombination epoch, the initial velocity of each baryonic shell at $z_i = 500$ is assumed to be the Hubble velocity $v_b(r) = Hr$. For the dark matter, we assume that the perturbation is dominated by the growing mode and choose the initial velocity for the dark matter shells accordingly, $v_{dm}(r) = Hr(1 - \frac{1}{3}\langle\delta_{dm}\rangle_r)$.

The initial relative abundances and mass fractions of the various species are taken to be the following: $x_{H^+} = x_e = 10^{-4}$ (see Peebles 1993), $x_{H_2} = 1.7 \times 10^{-6}$ (see Palla et al. 1983), $x_{H^-} = x_{He^+} = x_{He^{++}} = x_{H_2^+} = 0$, and $y_H + y_{H^+} + y_{H_2} + y_e = 0.76$, $y_{He} = 0.24$. Note that the freeze out value of the electron fraction scales with the cosmological parameters as $x_e \propto \Omega_0^{1/2}\Omega_b^{-1}h^{-1}$.

4.2. Definitions of "Collapse" and "Object"

In order to express the state of the gas as a function of the initial conditions, we need to define what we mean by the concepts of "collapse" and "object." We base our heuristic definitions on the spherical top-hat collapse model (Gunn

TABLE 1
ROOT MEAN SQUARE FLUCTUATION $\sigma(M)^a$

M_{cloud} ($M_\odot$)	$\sigma_{dm}(M, z = 500)$	
	Top-Hat	Gaussian
50	0.118	0.113
100	0.115	0.110
500	0.107	0.103
1000	0.104	0.100
5000	0.097	0.093
10^4	0.093	0.090

^{a} Given in two different-shaped filters with the COBE-normalized ($\sigma_{8\,h^{-1}\,Mpc} = 1.22$) BBKS power spectrum of a CDM universe at $z = 500$.

& Gott 1972). In this model, virialization occurs at half the turnaround radius when the overdensity is ~100–200. The value appears to be rather insensitive to the underlying cosmology (see Fig. 4 in Richstone, Loeb, & Turner 1992). We therefore define a shell to have *collapsed* if the average overdensity enclosed by that shell is $\bar{\delta}_b \geq \bar{\delta}_{thr} = 200$.

As time evolves, the density profile within the collapsing region steepens, and at some definite time, the average density contrast within the innermost baryonic shell reaches the threshold value $\bar{\delta}_b(r_1) = \bar{\delta}_{thr} = 200$. The subsequent shells reach this threshold some time later. We define an *object* to include all the baryonic material within the outermost shell that has collapsed. According to this definition, the mass of the object $M_{obj}(z)$ is zero until the first shell reaches $\bar{\delta}_{thr} = 200$, and is monotonically increasing afterward.

Unlike definitions based on optical depth, or absolute density, the threshold overdensity does not strongly depend on the mass scale involved. In the presence of cooling we find our results to be rather insensitive to the exact value of the threshold overdensity (see below).

4.3. *Collapse without Dark Matter or Cooling*

The simplest system to consider consists of a purely baryonic cloud following adiabatic infall, without any dark matter or radiative processes. We present results from test cases of such a system in order to establish a prototype against which we will compare results later, when the dark matter component and the radiative processes will be added.

For the initial conditions (see § 4.1), it is necessary to fix two free parameters: the height of the density peak $\delta_{b,i}$, and the mass scale M_{cloud}, or equivalently, the width $\sim k^{-1}$ of the initial density peak. The density peak $\delta_{b,i}$ sets the redshift at which the perturbation reaches the nonlinear phase, and k determines the initial ratio of pressure to gravitational forces.

In Table 2 we summarize the parameters for eight different runs. The runs numbered 1–4 are purely baryonic and do not include any radiative cooling, while the runs numbered 5–8 contain a mixture of baryons and cold dark matter, and include radiative cooling.

We first discuss the results of the first four simulations. In Figure 4 we show the trajectories of 10 shells (enclosing 7%, 17%, 27%, ..., 87%, and 97% of the total baryonic mass M_{bound}) across the radius of the sphere (*solid curves*), along with the trajectories that each shell would have had if it were freely falling (*dashed curves*). In all cases, the baryonic

shells expand, turn around, collapse, shock, and then drift slowly toward the center. The trajectories of the shells are similar to the semianalytic solution of Bertschinger (1985). Here, however, the shells hit the shock at slightly different fractions of their turnaround radii rather than at the fixed fraction of $\frac{1}{2}$, because of corrections of order δ_i^2 to Bertschinger's results. The higher mass runs (1 and 3) initially follow the free-fall trajectories, but eventually deviate from them after the shells' shock. In the lower mass runs (2 and 4), pressure is important and the collapse is delayed relative to the free-fall case even before the shock. The temperature evolution for these shells is shown in Figure 5.

In Figure 6 we show the fraction of the total bound baryonic mass that has collapsed to form the object (*solid lines*). We also show what this collapsed fraction would be for a pressureless freely falling gas (*dotted lines*). The higher mass runs deviate from the free-fall curves only after the shocked shells collapse. In the lower mass runs, the collapse is delayed relative to the free-fall case at all times.

4.4. *Collapse with Dark Matter and Cooling*

Given some choice of cosmological parameters H_0, Ω_{dm}, and Ω_b, and the ratio $\delta_{b,i}/\delta_{dm,i}$, there are again only two free parameters left, namely, the initial baryonic cloud mass M_{cloud} and the amplitude $\delta_{dm,i}$. We have performed simulations on a grid in the $(M_{cloud}, \delta_{dm,i})$ parameter space. The details of the four simulations numbered 5–8 in Table 2 are shown in Figures 7–12.

Figure 7 shows the trajectories of 10 shells (enclosing 7%, 17%, 27%, ..., 87%, and 97% of the total baryonic mass M_{bound}). The trajectory of each shell is shown by a solid line, until the average density contrast within it reaches the threshold value $\bar{\delta}_{thr} = 200$. Once the overdensity within a shell reaches $\bar{\delta}_{thr}$, it is considered to be part of the central object. To indicate this in the plots, we continue to draw the shell trajectories as dotted lines after they reach $\bar{\delta} = \bar{\delta}_{thr}$. The dashed lines show the trajectories of the dark matter shells. In the smallest mass run (5), cooling is inefficient and the gas shells stop moving after they shock. In larger mass cases (runs 6 and 7), cooling is more efficient. Finally, in the largest mass case (run 8), all the shocked shells cool rapidly and fall toward the center.

Figure 8 shows the evolution of the temperature with redshift for the same gas shells. The dotted lines show the CBR temperature $T_\gamma \propto (1 + z)$, and the dashed lines show the adiabatic temperature scaling in the linear regime $T_{ad} \propto (1 + z)^2$. The temperature of the gas remains approximately uniform initially, with a value in-between the adiabatic and

TABLE 2
Parameters of the Numerical Runs

Run Number	Baryon Mass M_{cloud} $(M_\odot)$	Height δ_i	Width R_{cloud} (pc)	Baryons Ω_b	Dark Matter Ω_{dm}	Cooling (Yes/No)
1	5×10^7	0.13	235.56	0.1	0	No
2	5×10^5	0.13	50.75	0.1	0	No
3	5×10^7	0.39	228.96	0.1	0	No
4	5×10^5	0.39	49.33	0.1	0	No
5	500	0.26	5.13	0.1	0.9	Yes
6	1000	0.26	6.46	0.1	0.9	Yes
7	1000	0.39	6.45	0.1	0.9	Yes
8	5000	0.26	11.05	0.1	0.9	Yes

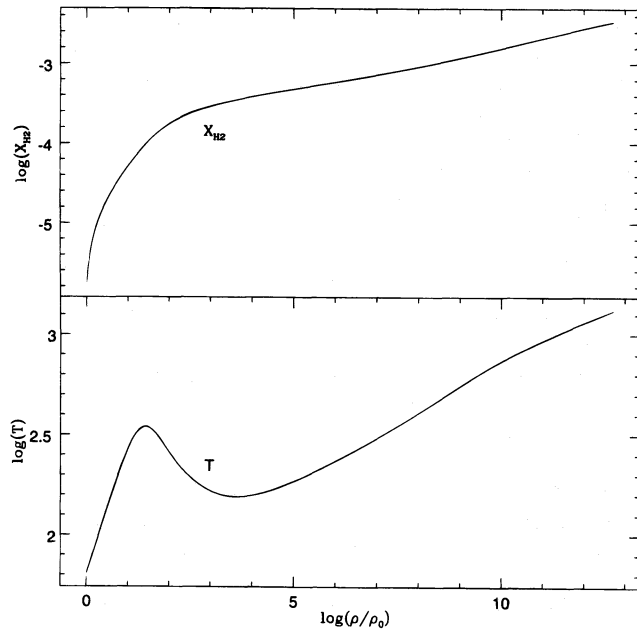NOTE.—Initial heights and widths are at $z = 500$.

FIG. 3.—Fractional abundance of H_2 molecules and temperature (in kelvins) vs. density in a freely collapsing uniform sphere in the presence of H_2 cooling. Parameters of the sphere are described in § 3.2 (3).

cooling, the temperature of each shell remains approximately constant, increasing slowly because of the slight adiabatic compression. When cooling is efficient, i.e., when the cooling time becomes smaller than the dynamical time, the temperature reaches a maximum value and then decreases very quickly (see run 8 in Fig. 8). The temperature at which this turnover occurs in our simulations is of the order $\log (T/K) \approx 2.3$–2.8 at the onset of H_2 cooling. Figure 9 shows the evolution of the four most efficient cooling and heating terms with redshift in a typical run. The most efficient radiative mechanism before the shock (when the temperature of the gas is below the temperature of the CBR) is Compton heating; this process keeps the gas temperature above T_{ad}. After the shock, the most efficient radiative mechanism is H_2 cooling, causing a turnover in the temperature. Note that the gas temperature reaches a value above T_γ, so that the H_2 molecules as well as Compton scattering cool the gas, rather than heat it. After the temperature starts to decline, the shells fall toward the center essentially at the free-fall rate. When the shells reach a very small radius and the numerical time step necessary to resolve their motion becomes too small, we artificially set the temperature of these shells to $T = 200$ K and subsequently ignore them.

Figure 10 shows the evolution of the relative abundances of H_2 and e^- within five different shells in the central region (enclosing 2%, 7%, 12%, 17%, and 22% of the total baryonic mass M_{bound}). The highest relative abundance of H_2 is achieved in the case of the largest perturbed mass (run 8), where it reaches about 10^{-3}. The abundances develop a

CBR cases. After turnaround the temperature increases adiabatically and a temperature gradient develops. Eventually, as each shell encounters the shock, its temperature jumps abruptly to the virial temperature. In the absence of
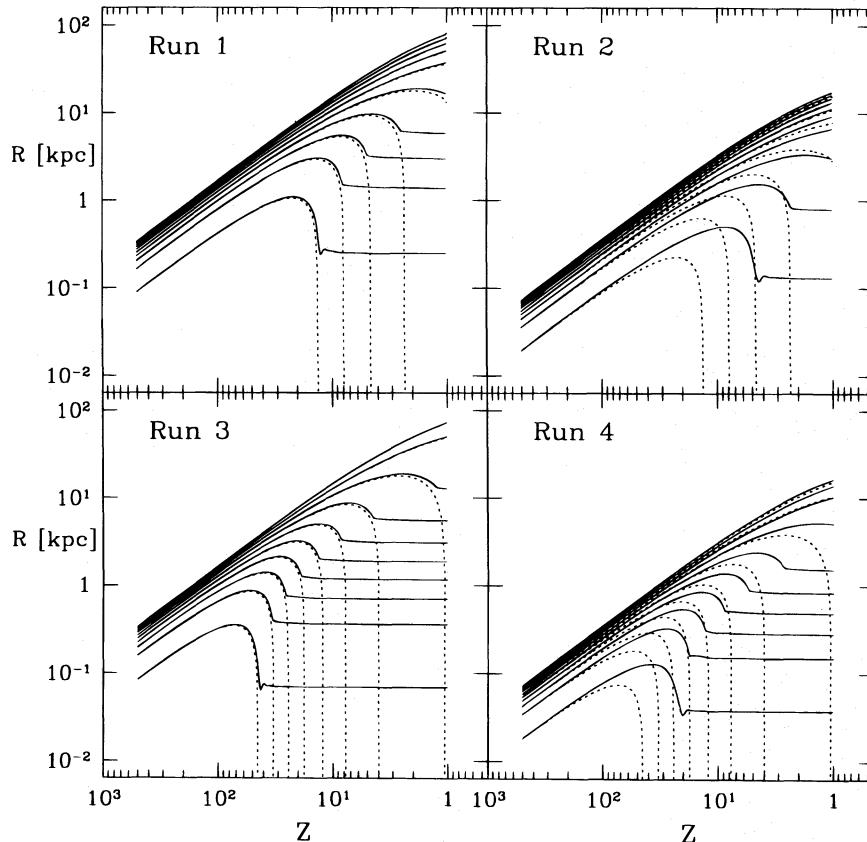

FIG. 4.—Evolution of the (physical) radii of 10 gas shells (enclosing 7%, 17%, 27%, ..., 87%, and 97% of the total baryonic mass M_{bound}) for four pure baryonic runs without cooling. The parameters of these runs are summarized in Table 2. The solid lines show the shell trajectories from the simulations, while the dashed lines show for reference the corresponding shell trajectories for a pressureless gas.
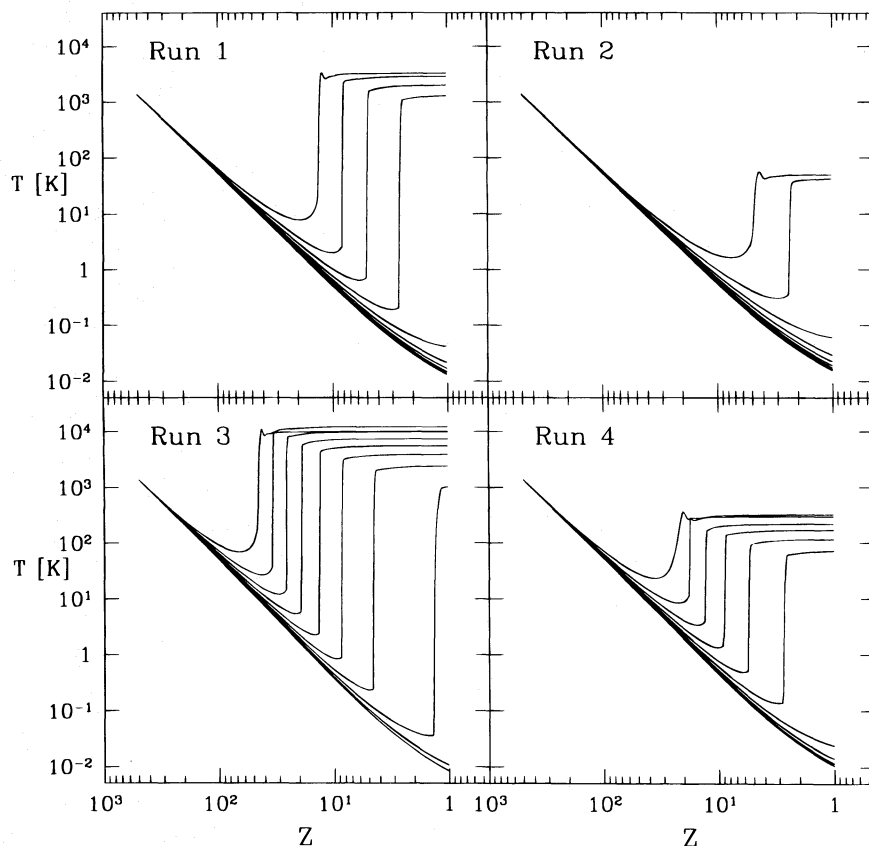
FIG. 5.—Temperature evolution of the gas shells that appear in Fig. 4

gradient across the sphere, which is positive for H_2 and negative for the electrons. The evolutions of the abundances are relatively universal and look similar in all four runs. In particular, $\log x_{H_2} \approx -3.6$ in all four runs before the gra-

FIG. 6.—Fraction of the bound mass that has collapsed as a function of redshift for the four runs 1–4 in Table 2 (*solid lines*). The two dashed lines show what the collapsed baryonic mass fraction would be in each case if the cloud had been in free-fall. The line marked "A" is for $\delta_{dm,i} = 0.13$ (to be compared with runs 1 and 2) and the line marked "B" is for $\delta_{dm,i} = 0.39$ (to be compared with runs 3 and 4).

dient develops, and the central value is $\log x_{H_2} \approx -3.2$ afterward. The main difference between the four runs is the redshift at which the gradients develop.

Figure 11 shows typical density, temperature, and relative H_2 and e^- abundance profiles across the sphere at redshift $z = 10$ for each of the four runs. The x_{H_2} profiles are almost flat at the outer part of the sphere, and well approximated by a power law $x_{H_2} \propto r^{-0.4}$ within the postshock region, while the e^- fraction profiles behave less regularly. Note that the power-law profile for the density $\rho \propto r^{-2.25}$ predicted by the self-similar solution (Bertschinger 1985) is obtained near the center (see § 2 and the thick line in Fig. 11a).

Figure 12 shows the fraction of the collapsed baryonic mass out of the total bound baryonic mass versus redshift for the runs 5–8, for two different values of the overdensity threshold for forming objects $\bar{\delta}_{thr}$. The collapsed baryonic mass versus redshift curves are rather insensitive to the value of $\bar{\delta}_{thr}$, especially for the objects that collapse early.

4.5. Collapse onto a Black Hole

Next, we perform the same runs as described in § 4.4, but with a different central boundary condition; we replace the reflecting hard sphere with a black hole sink of a fixed radius. We choose the radius of the sink to be a small fraction of the initial radius of the first shell. The shells that cross the black hole radius are assigned arbitrary values of density and temperature, and are subsequently ignored. Under these conditions, the dark matter component does not bounce back and virialize, since it is absorbed by the central black hole. Due to the postshock shell crossing, the gas component continues to collapse after it shocks, unlike
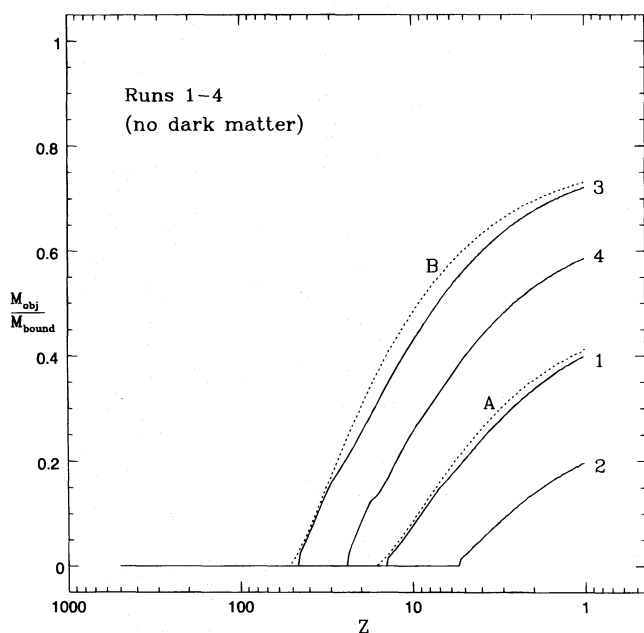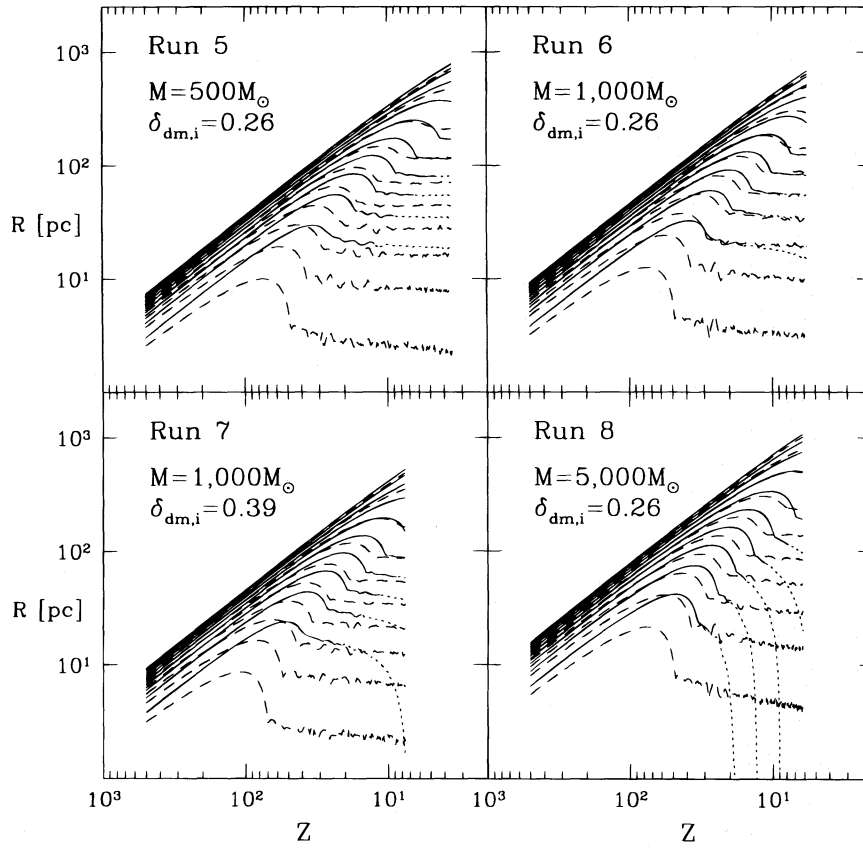
FIG. 7.—Evolution of the (physical) radii of 10 gas shells (enclosing 7%, 17%, 27%, ..., 87%, and 97% of the total baryonic mass M_{bound}) for four mixed baryons and dark matter runs with cooling. The parameters of these runs, numbered 5–8, are summarized in Table 2. The trajectories of dark matter shells are shown as dashed lines. The trajectories of the gas shells are shown as solid lines until they reach $\bar{\delta} = \bar{\delta}_{thr}$, and as dotted lines afterward.
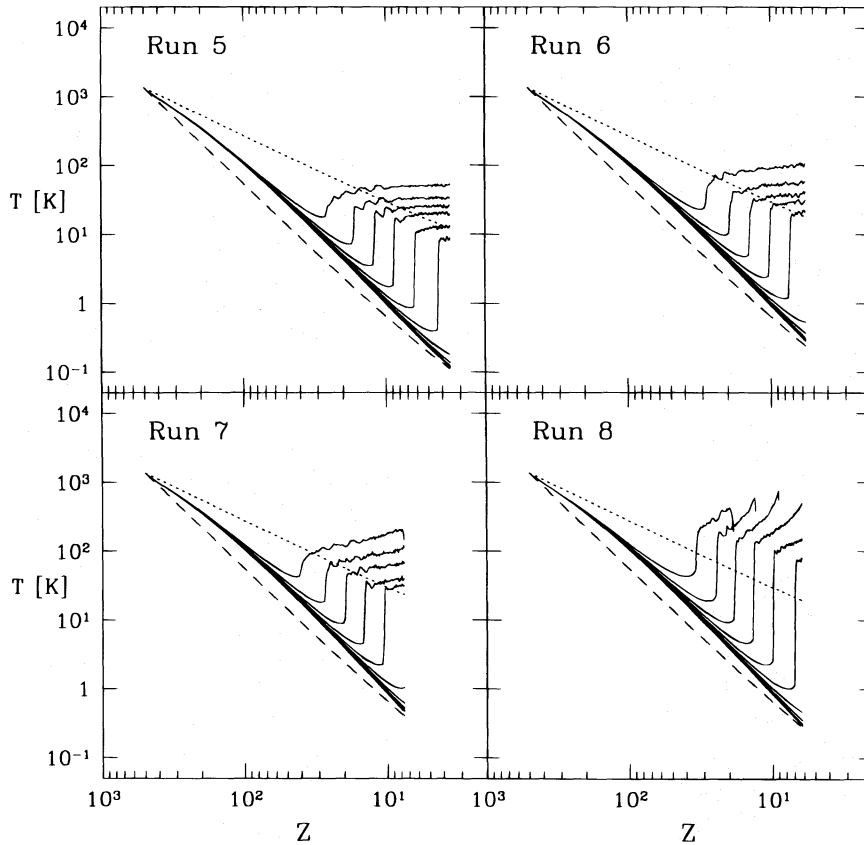

FIG. 8.—Temperature evolution of the gas shells that appear in Fig. 7. The dotted lines show the CBR temperature $T_\gamma \propto (1 + z)$, and the dashed lines show the adiabatic temperature $T_{ad} \propto (1 + z)^2$. The gas temperature remains between T_γ and T_{ad} until it shocks.
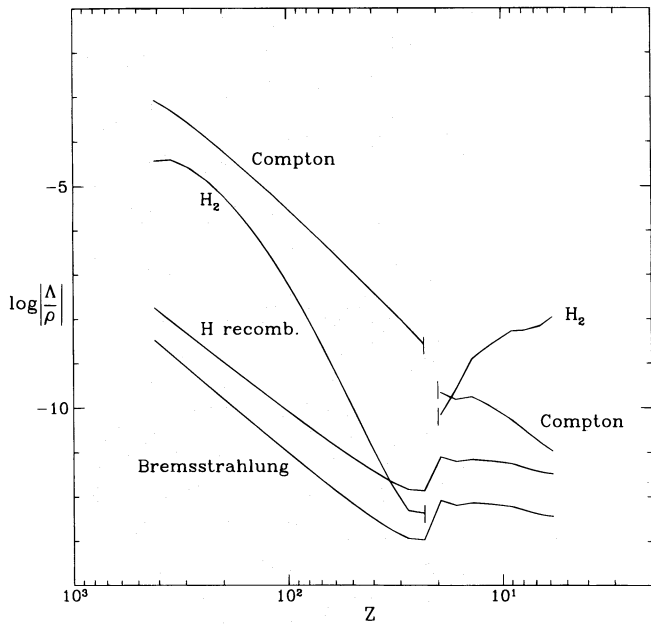
FIG. 9.—Redshift evolution of the four most efficient radiative cooling/heating terms within the shell enclosing 12% of the total baryonic mass M_{bound} in a typical run (6). Before the gas temperature rises above the CBR temperature, both Compton scattering and the radiative transitions of H_2 heat the gas. Λ changes sign for these processes in-between the tick marks. After $T_b > T_\gamma$ (or $z \lesssim 22$), both of these mechanisms cool the gas; the most efficient postshock cooling is due to H_2. The units of Λ/ρ are ergs $s^{-1} g^{-1}$.

in the case of a reflecting sphere. This continued collapse and compression lead to a continuous rise in the gas density and temperature after the shock. The increased gas density and temperature enable more efficient postshock cooling.

In the presence of a central black hole, we have found an oscillatory instability of the shock front in the cases involving efficient radiative cooling. Instead of propagating outward monotonously as in the cases shown in Figure 7, the shock front in these cases can reverse its motion and oscillate. However, for the present application, the details of these oscillations can be glossed over, since we are only interested in the question whether shells reach $\bar{\delta} = \delta_{thr}$. The oscillation of the shock front occurs only for shells that have already collapsed according to our definition, hence this instability affects only the structural details of the objects we find but not the question of whether they form.

4.6. Discussion

We next explore the $(M_{cloud}, \delta_{dm,i})$ parameter space for the two different boundary conditions. In each case, we determine whether radiative cooling affects the dynamics of the gas and whether an object forms.

To assess the significance of cooling in each run, we compared the trajectories of the gas shells with and without cooling. If the trajectories in the two cases were indistinguishable, we concluded that cooling had no effect; if they differed significantly, we concluded that cooling was efficient. To establish whether or not an object formed, we used
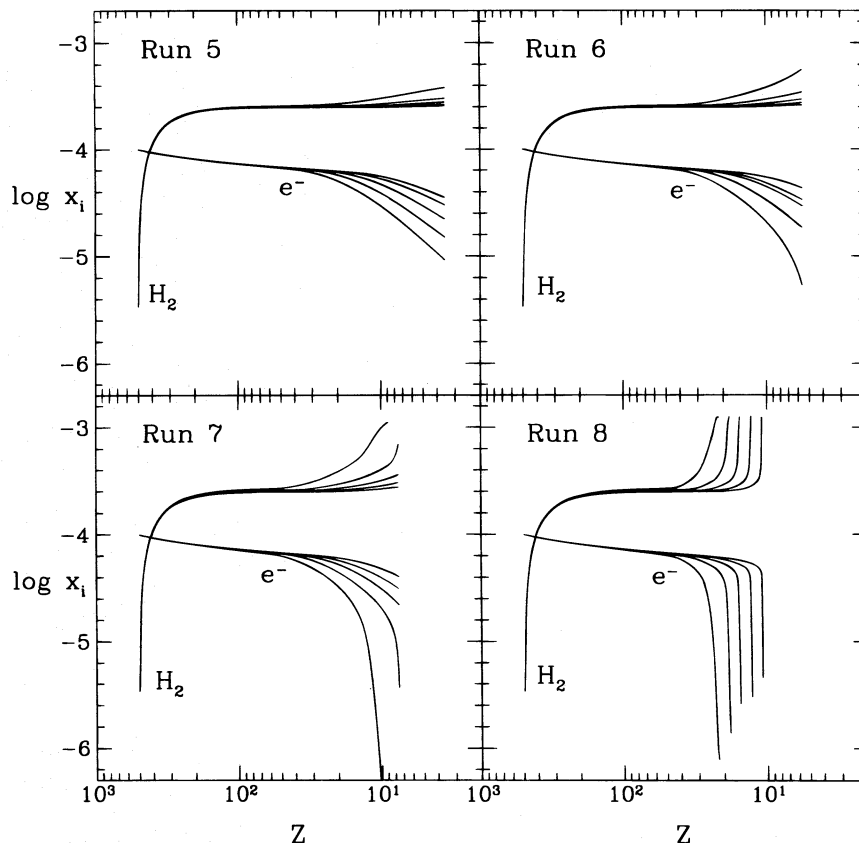

FIG. 10.—Evolution of the relative abundances of H_2 and e^- for five shells (enclosing 2%, 7%, 12%, 17%, and 23% of the total baryonic mass M_{bound}) in runs 5–8.
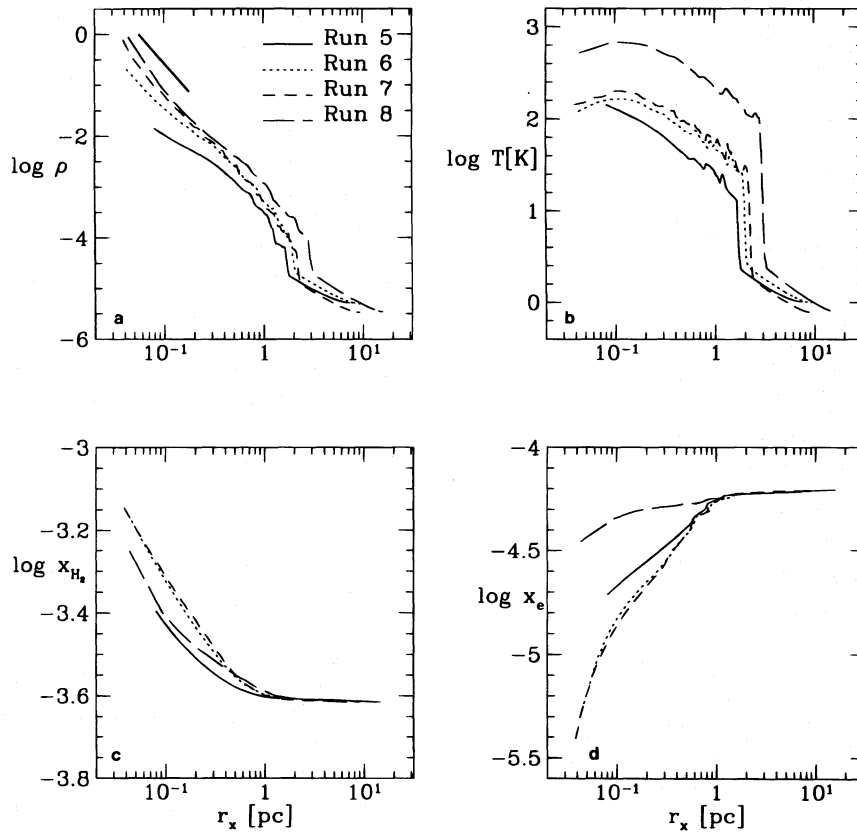
FIG. 11.—(a–d) Density, temperature, relative H_2 abundance profile, and e^- abundance profile, respectively, in runs 5–8 at redshift $z = 10$. The abscissa is the comoving radius $r_x = R(1 + 500)/(1 + z)$, where R is the physical radius. The density ρ is given in units of $M_\odot$ pc^{-3}. The thick line on the top left corner of panel a shows the slope of the density profile in the pressureless self-similar solution (Bertschinger 1985).

a simple criterion: for an object to form, we required that at least half of the baryonic mass within the original cloud should collapse by a redshift $z = 10$, i.e., $M_{obj}(z = 10)/M_{cloud} \geq 1/2$. This corresponds to one-sixth of the total

bound mass (M_{bound}) being above a density contrast of 200. The choice of $z = 10$ in the above definition is somewhat arbitrary; we show how our results change with different choices of z in Figures 6 and 12.

The main parameters that determine the postshock cooling rate are the virial temperature T_{vir} and the abundance of molecular hydrogen x_{H_2} after the shock. While it is not possible to calculate x_{H_2} analytically, the scaling of the virial temperature can be derived from the spherical top-hat model (White 1994). Using our runs with a central hard sphere to calibrate this relation for the baryons, we find that for $\Omega_0 = \Omega_b + \Omega_{dm} = 1$, the postshock temperature of the gas shells closely follow

$$T_{vir} = 55(1 + z_s)\left(\frac{h}{0.5}\right)^{2/3}\left(\frac{M_{cloud}}{10^5 M_\odot}\right)^{2/3} \text{K} , \quad (19)$$

where z_s is the shock redshift of each gas shell and M_{cloud} is the baryonic mass of the cloud. The postshock values for x_{H_2} do not vary substantially between runs, as shown in Figure 10.

In Figure 13 we show the grid of points we explored in the (M_{cloud}, $\delta_{dm,i}$) parameter space. The solid lines correspond to lines of constant central virial temperatures, $T_{vir} = 85$ K and $T_{vir} = 120$ K. The solid circles on this grid represent cases where cooling had no effect; the open circles represent cases where cooling was very efficient; and the open triangles represent intermediate cases, where cooling had a small but noticeable effect. The (M_{cloud}, $\delta_{dm,i}$)-plane can be divided into two regions: the region where cooling is important and the region where cooling is not important.
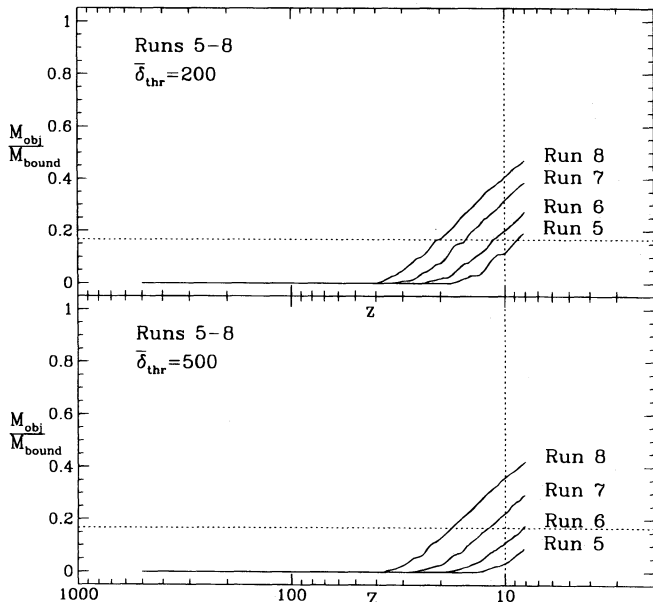

FIG. 12.—Fraction of the total baryonic bound mass that has collapsed and formed an object in runs 5–8 vs. redshift. The upper panel shows results with $\bar{\delta}_{thr} = 200$, the lower panel with $\bar{\delta}_{thr} = 500$. The vertical and horizontal dashed lines illustrate the condition $M_{obj}/M_{cloud} \geq 0.5$ (or, equivalently, $M_{obj}/M_{bound} \geq 0.17$) at $z = 10$.
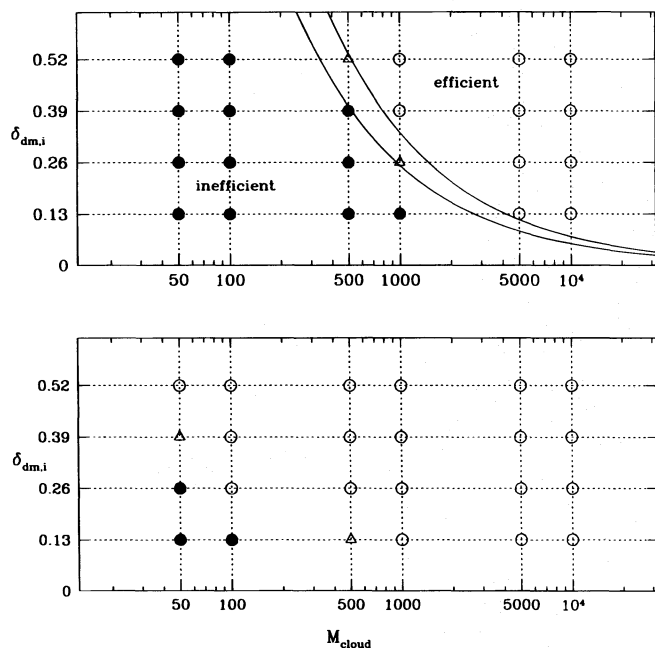
FIG. 13.—Effectiveness of radiative cooling as a function of the two parameters M_{cloud} and $\delta_{dm,i}$. Filled circles represent cases where cooling had no effect; open circles denote cases where cooling was very efficient; open triangles represent intermediate cases where cooling had a minor but noticeable effect. On these mass scales, $\delta_{dm,i} = 0.13$ corresponds to 1.1–1.4 σ for the *COBE*-normalized ($\sigma_8 = 1.22$) cold dark matter power spectrum (see Table 1). The upper panel refers to runs with a reflecting sphere in the center, and the lower panel to runs with a central black hole. The solid curves are lines of constant virial temperature (see eq. [19]); the upper and lower curves correspond to temperatures of 120 and 85 K, respectively.

FIG. 14.—Collapse as a function of the two parameters M_{cloud} and $\delta_{dm,i}$. The definition of "collapse" is given in § 4.2. Filled circles represent runs where none of the shells have collapsed by the redshift $z = 10$; open circles represent runs where more than half of the baryonic mass M_{cloud} has collapsed by $z = 10$; open triangles represent intermediate cases where only the innermost few shells have collapsed. The upper panel refers to runs with a reflecting sphere in the center, and the lower panel to runs with a central black hole. The solid lines are curves of constant virial temperature, as in Fig. 13.

According to our results, this division follows roughly a line of constant virial temperature, $T_{vir} \sim 10^2$ K.

In Figure 14 we show again the above grid of points, but here the solid dots represent cases where no object formed by $z = 10$: the open dots represent cases where objects formed by $z = 10$; and the triangles represent intermediate cases, where objects are just starting to form at $z = 10$. Again, we can divide the (M_{cloud}, $\delta_{dm,i}$)-plane into two regions, depending on whether objects form or not. The constant T_{vir} curves from Figure 13 are also overlayed on this plane. According to the upper panel, we see that the division based on cooling goes through points of somewhat higher $\delta_{dm,i}$ than the division based on collapse in the case of a central reflecting sphere. In other words, the transition from "no collapse" to "collapse" takes place in a regime where cooling is ineffective. Thus, radiative cooling does not introduce new mass or overdensity scales that are able to collapse.

The above result can be understood physically as follows. In order for H_2 cooling to affect the dynamics, the gas temperature T_b must satisfy two conditions. First, in order for cooling (rather than heating) to occur, the gas temperature must be higher than the CBR temperature. Second, the H_2 cooling time needs to be smaller than the typical dynamical time; we find that this is only possible for a temperature $T_b \gtrsim 10^2$ K. We find that the above two conditions cannot be satisfied simultaneously before the gas shocks. The gas temperature drops below 10^2 K as early as $z \sim 100$, before any object forms, and rises above 10^2 K again only after the gas shocks (see Fig. 8). However, by that late time the gas has already achieved an overdensity
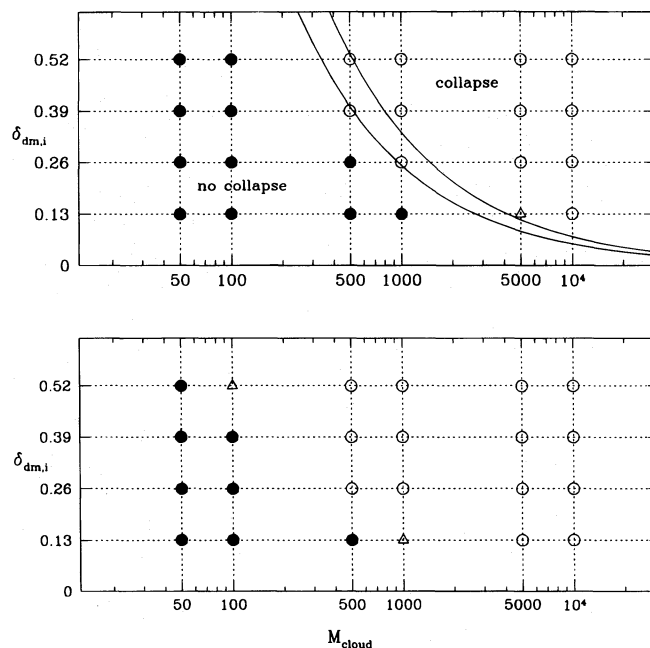
close to our collapse criterion $\bar{\delta} \sim 200$. Thus, even if cooling alters the postshock trajectories significantly (as in run 8 in Fig. 7), its effect translates into a minor change in the collapsed baryonic mass as a function of redshift, $M_{obj}(z)$.

The situation is somewhat different for collapses with a central sink (black hole) boundary condition. In the hard sphere case, the dark matter shells bounce back from the center, virialize, and stop moving subsequently. After a gas shell shocks, it is not crossed by dark matter shells, unless radiative cooling is sufficiently effective to reduce its pressure support and allow it to fall toward the center. In the central sink case, the dark matter shells do not bounce back and virialize; instead, they are absorbed by the sink. Even after a gas shell shocks, it is crossed continuously by new dark matter shells. Therefore, gas shells continue to collapse after they shock even in the absence of radiative cooling. The continued infall heats the gas adiabatically, and the importance of postshock cooling is enhanced relative to the hard sphere case. The lower panel of Figure 13 shows that cooling is indeed effective for much smaller mass scales than in the hard sphere case; the gas dynamics in clouds with a baryonic mass as low as $M_{cloud} = 10^2$–10^3 $M_\odot$ is altered by cooling. For higher mass runs, H_2 cooling becomes so effective as to smooth out the shocks; the gas shells fall in rapidly, and their trajectories show little evidence for a discontinuity. The cooling effects change the collapsed baryonic mass as a function of redshift, $M_{obj}(z)$ and allow slightly lower mass scales to collapse by $z = 10$. Indeed, the lower panel of Figure 14 shows that the transition from "no collapse" to "collapse" occurs for slightly lower masses than in the hard sphere case, and in a regime where cooling is efficient.

5. CONCLUSIONS

In this paper we have investigated the early ($z \gtrsim 10$) formation of bound objects with masses in baryons comparable to the linear theory Jeans mass ($\sim 10^5 \ M_\odot$). We used a spherically symmetric Lagrangian code to analyze the dynamics of low-mass overdense regions in a cold dark matter cosmology. The code solved for the radial trajectories of the dark matter and gas shells, along with the density, temperature, and nonequilibrium abundances of various chemical ingredients of the gas in each shell.

The dynamics of a primordial gas cloud depends primarily on two parameters: the baryonic mass ($M_{\rm cloud}$) and the initial overdensity ($\delta_{{\rm dm},i}$) of the cloud. We have computed the evolution of gas clouds on a grid of 48 runs, corresponding to different points in the ($M_{\rm cloud}, \delta_{{\rm dm},i}$) parameter space. We have done the calculations with two different types of central boundary conditions for the dark matter: a reflecting hard sphere and a central sink (black hole).

Based on the above grid of runs, one can study the effect of radiative cooling by molecular hydrogen (H_2) on the dynamics of the baryons. We find that, in the hard sphere case, H_2 cooling is important only when the virial temperature of the collapsing object is $\gtrsim 100$ K (see eq. [19] and Fig. 13). However, this temperature regime is accessible only after shock heating, when the gas has already condensed to be part of a nonlinear object. Before the gas enters the virialization shock, its temperature is lower than the CBR temperature and radiative H_2 cooling is not possible. This implies that contrary to previous suggestions, radiative cooling could not have triggered the formation of the first generation of bound objects in the universe.

However, the evolution of the gas after it shocks can be substantially altered as a result of H_2 cooling. This effect is particularly emphasized in the case of a central sink boundary condition (see lower panel of Fig. 13), where the dark matter shells cross the baryonic shells and pull them effectively toward the center. This process brings the baryonic shells to a thermodynamic state that favors efficient cooling.

In general, we find that the presence of shell crossing by dark matter allows baryonic objects with masses well below the linear theory Jeans mass to form. Figures 7 and 14 demonstrate that the cores of objects containing $\lesssim 10^3 \ M_\odot$ in baryons can collapse in a standard CDM cosmology by a redshift $z = 10$. It is therefore possible that high-mass stars had formed in the intergalactic space directly as a result of the primordial cosmological perturbations, and not just due to the commonly discussed process of fragmentation inside more massive objects. Intergalactic stars may have left their signature on the metallicity of the intergalactic medium and of Lyα absorption clouds through supernovae at high redshifts. It is difficult to detect the light from intergalactic stars unless they are assembled into high–surface brightness objects. However, such stars should result in gravitational microlensing events of quasars, with a lensing probability comparable to their cosmological density parameter $\sim \Omega_*$ (Press & Gunn 1973).

The most significant limitation of our approach is the assumption of spherical symmetry. This assumption is forced upon us by practical computational considerations. Spherical symmetry may, in fact, apply to the collapse of a small subset of systems in environments with unusually low shear (Eisenstein & Loeb 1995b). However, most three-dimensional collapses are likely to be triaxial (Eisenstein & Loeb 1995a, and references therein). The early pancaking along the short axis would enhance the gas density and the corresponding H_2 formation, and could lead to a more efficient cooling of the gas. Fragmentation may lead to similar effects (see Ruzmaikina 1973; Kashlinsky & Rees 1983). Future three-dimensional simulations are essential in exploring this more complicated dynamics.

APPENDIX A

COOLING AND HEATING TERMS

The cooling terms in Λ of equation (9) in § 3.1 are given by the sum of the following 12 terms below, in units of ergs s^{-1} cm^{-3}. References are Black (1981) and Cen (1992) for the first 10 terms, Spitzer & Hart (1971) for the Gaunt factor $g_{\rm ff}$ appearing in $\Lambda_{\rm Brem}(T)$, Shapiro & Kang (1987) for $\Lambda_{\rm Comp}(T)$, and Lepp & Shull (1983) for $\Lambda_{H_2}(T)$. In these formulas, T denotes the gas temperature in kelvins, and T_γ is the temperature of the CBR, $T_\gamma = 2.726(1 + z)$ K. The number densities, n_i, are in cm^{-3}.

Collisional ionization of H, He, and He$^+$:

$$\Lambda_{\rm H}(T) = 1.27 \times 10^{-21} T^{1/2}(1 + T_5^{1/2})^{-1} \exp(-157{,}809.1/T) n_e n_{\rm H} \,,$$

$$\Lambda_{\rm He}(T) = 9.38 \times 10^{-22} T^{1/2}(1 + T_5^{1/2})^{-1} \exp(-285{,}335.4/T) n_e n_{\rm He} \,,$$

$$\Lambda_{\rm He^+}(T) = 4.95 \times 10^{-22} T^{1/2}(1 + T_5^{1/2})^{-1} \exp(-631{,}515/T) n_e n_{\rm He^+} \,.$$

Recombination to H, He, and He$^+$:

$$\Lambda_{\rm H^+}(T) = 8.70 \times 10^{-27} T^{1/2} T_3^{-0.2}(1 + T_6^{0.7})^{-1} n_e n_{\rm H^+} \,,$$

$$\Lambda_{\rm He^+}(T) = 1.55 \times 10^{-26} T^{0.3647} n_e n_{\rm He^+} \,,$$

$$\Lambda_{\rm He^{++}}(T) = 3.48 \times 10^{-26} T^{1/2} T_3^{-0.2}(1 + T_6^{0.7})^{-1} n_e n_{\rm He^{++}} \,.$$

Dielectric recombination to He:

$$\Lambda_{\text{He}^+}(T) = 1.24 \times 10^{-13} T^{-1.5} \exp(-470{,}000/T)[1 + 0.3 \exp(-94{,}000/T)]n_e n_{\text{He}^+} .$$

Collisional excitation of H and He$^+$:

$$\Lambda_{\text{H}}(T) = 7.50 \times 10^{-19}(1 + T_5^{1/2})^{-1} \exp(-118{,}348/T)n_e n_{\text{H}} ,$$

$$\Lambda_{\text{He}^+}(T) = 5.54 \times 10^{-17} T^{-0.397}(1 + T_5^{1/2})^{-1} \exp(-473{,}638/T)n_e n_{\text{He}^+} .$$

Bremsstrahlung:

$$\Lambda_{\text{Brem}}(T) = 1.42 \times 10^{-27} g_{\text{ff}} T^{1/2} n_e(n_{\text{H}^+} + n_{\text{He}^+} + 4n_{\text{He}^{++}}) ,$$

$$g_{\text{ff}} = 1.10 + 0.34 \exp[-(5.50 - \log T)^2/3.0] .$$

Compton cooling:

$$\Lambda_{\text{Comp}}(T) = 1.017 \times 10^{-37} T_\gamma^4(T - T_\gamma)n_e .$$

Cooling due to H$_2$ *molecules.*—A lengthy expression for the term $\Lambda_{\text{H}_2}(T)$ was adopted from Lepp & Shull (1983). The expression in this reference is an analytical fit to the authors' numerical results. It includes cooling from the following mechanisms involving H$_2$:

1. Dissociation of H$_2$ molecules from H$_2$-H$_2$ collisions,
2. Dissociation of H$_2$ molecules from H$_2$-H collisions,
3. De-excitation from excited rotational and vibrational states, due to H$_2$-H$_2$ collisions,
4. De-excitation from excited rotational and vibrational states, due to H$_2$-H collisions.

However, radiative cooling by H$_2$ is not possible thermodynamically when $T < T_\gamma$; instead, H$_2$ is a source of heating under this condition. In order to correct for the presence of radiative heating from the inverse of the above processes, we multiply the quoted value $\Lambda_{\text{H}_2}(T)$ by the factor $(T - T_\gamma)/(T + T_\gamma)$. This factor has the correct limiting values ± 1 for $T \gg T_\gamma$ and $T \ll T_\gamma$, respectively. Note that there is a typographical error in Lepp & Shull 1983 (confirmed by S. Lepp 1995, private communication), which changes the value of $\Lambda_{\text{H}_2}(T)$ considerably. In their equation (8) on page 581, 1.10×10^{-13} should be replaced by 1.10×10^{-18}.

APPENDIX B

REACTION RATES AND CROSS SECTIONS

Table 3 lists the chemical reactions included in equations (12) in § 3.1. We attempted to include all possibly important reactions. The rates for reactions (5), (7), (15), (16), and (21) and the cross section for reaction (27) are given by more lengthy expressions, which can be found in the references. The expression for the cross section in reaction (26) is a fit to the data from Stancil (1994), with temperature-dependent coefficients p_i. The coefficients α, β, v_T, and s appearing in the cross sections for reactions (22)–(25) can be found in Osterbrock (1974).

TABLE 3

A. REACTION RATES

Reaction	Rate Coefficient (cm^3 s^{-1})	Reference
(1) H + e^- → H$^+$ + 2e^-	$5.85 \times 10^{-11} T^{1/2} \exp(-157{,}809.1/T)(1 + T_5^{1/2})^{-1}$	1
(2) He + e^- → He$^+$ + 2e^-	$2.38 \times 10^{-11} T^{1/2} \exp(-285{,}335.4/T)(1 + T_5^{1/2})^{-1}$	2
(3) He$^+$ + e^- → He^{++} + 2e^-	$5.68 \times 10^{-12} T^{1/2} \exp(-631{,}515.0/T)(1 + T_5^{1/2})^{-1}$	1
(4) H$^+$ + e^- → H + hv	$8.40 \times 10^{-11} T^{-1/2} T_3^{0.2}(1 + T_6^{0.7})^{-1}$	1
(5) He$^+$ + e^- → He + hv	See expression in reference	1
(6) He^{++} + e^- → He$^+$ + hv	$3.36 \times 10^{-10} T^{-1/2} T_3^{-0.2}(1 + T_6^{0.7})^{-1}$	1
(7) H + H$^+$ → H$_2^+$ + hv	See expression in reference	3
(8) H$_2^+$ + H → H$_2$ + H$^+$	6.40×10^{-10}	4
(9) H + e^- → H$^-$ + hv	$5.57 \times 10^{-17} T^{1/2}$	5
(10) H + H$^-$ → H$_2$ + e^-	1.30×10^{-9}	6
(11) H$_2^+$ + e^- → 2H	$1.68 \times 10^{-8}(T/300)^{-0.29}$	7
(12) H$_2^+$ + H$^-$ → H$_2$ + H	$5.00 \times 10^{-6} T^{-1/2}$	8
(13) H$^-$ + H$^+$ → 2H	$7.00 \times 10^{-7} T^{-1/2}$	8
(14) H$_2$ + e^- → H + H$^-$	$2.70 \times 10^{-8} T^{-3/2} \exp(-43{,}000/T)$	9
(15) H$_2$ + H → 3H	See expression in reference	10
(16) H$_2$ + H$_2$ → H$_2$ + 2H	See expression in reference	10
(17) H$_2$ + H$^+$ → H$_2^+$ + H	$2.4 \times 10^{-9} \exp(-21{,}200/T)$	11
(18) H$_2$ + e^- → 2H + e^-	$4.38 \times 10^{-10} \exp(-102{,}000/T)T^{0.35}$	11
(19) H$^-$ + e^- → H + 2e^-	$4.00 \times 10^{-12} T \exp(-8750/T)$	11
(20) H$^-$ + H → 2H + e^-	$5.30 \times 10^{-20} T \exp(-8750/T)$	11
(21) H$^-$ + H$^+$ → H$_2^+$ + e^-	See expression in reference	11

TABLE 3—*Continued*

B. Reaction Cross Sections

Reaction	Cross Section (cm^2)	Reference
(22) $H + h\nu \rightarrow H^+ + e^-$		
(23) $He + h\nu \rightarrow He^+ + e^-$	$\sigma(\nu) = a[\beta(\nu/\nu_T)^{-s} + (1-\beta)(\nu/\nu_T)^{-s-1}]$, $\nu \geq \nu_T$	12
(24) $He^+ + h\nu \rightarrow He^{++} + e^-$		
(25) $H^- + h\nu \rightarrow H + e^-$		
(26) $H_2^+ + h\nu \rightarrow H + H^+$	$\sigma(\nu, T) = (p_1 + p_2\nu) \exp[(\nu - p_3)^2/2p_4^2]$	13
(27) $H_2 + h\nu \rightarrow H_2^+ + e^-$	See expression in reference	11
(28) $H_2 + h\nu \rightarrow 2H$	$\sigma(\nu) = 3 \times 10^{-22}$, 11.26 eV $< h\nu < 13.6$ eV	14

REFERENCES.—(1) Cen 1992; (2) Black 1978; (3) Rawlings, Drew, & Barlow 1993; (4) Karpas, Anicich, & Huntress 1979; (5) Rawlings 1988; (6) de Jong 1972; (7) Nakashima, Takayi, & Nakamura 1987; (8) Dalgarno & Lepp 1987; (9) Hirasawa 1969; (10) Lepp & Shull 1983; (11) Shapiro & Kang 1987; (12) Osterbrock 1974; (13) Stancil 1994; (14) Hollenbach & McKee 1979.

REFERENCES

Bardeen, J. M., Bond, J. R., Kaiser, N., & Szalay, A. S. 1986, ApJ, 304, 15 (BBKS)
Bertschinger, E. 1985, ApJS, 58, 39
Binney, J., & Tremaine, S. 1987, Galactic Dynamics (Princeton: Princeton Univ. Press)
Black, J. H. 1978, ApJ, 222, 125
———. 1981, MNRAS, 197, 553
Blumenthal, G. R., Faber, S. M., Primack, J. R., & Rees, M. J. 1984, Nature, 311, 517
Bunn, E. F., Scott, D., & White, M. 1995, ApJ, 441, L9
Cen, R. 1992, ApJ, 78, 341
Cen, R., & Ostriker, J. P. 1994, ApJ, 431, 451
Couchman, H. M. P. 1985, MNRAS, 214, 137
de Jong, T. 1972, A&A, 20, 263
Dalgarno, A., & Lepp, S. 1987 in Astrochemistry, ed. M. S. Varya & S. P. Tarafdar (Dordrecht: Reidel), 109
Eisenstein, D. J., & Loeb, A. 1995a, ApJ, 439, 520
———. 1995b, ApJ, 443, 11
Evrard, A. E., Summers, F. J., & Davis, M. 1994, ApJ, 422, 11
Fan, X. M. 1994, Ph.D. thesis, Columbia Univ.
Frenk, C. S., et al., ed. 1989, The Epoch of Galaxy Formation (Dordrecht: Kluwer)
Gott, J. R. 1975, ApJ, 201, 296
Gunn, J. E., & Gott, J. R. 1972, ApJ, 176, 1
Haiman, Z., & Loeb, A. 1996, in preparation
Hernquist, L., Katz, N., & Weinberg, D. 1995, ApJ, 442, 57
Hindmarsh, A. C. 1983, in Scientific Computing, ed. R. S. Stepleman & M. Carver (Amsterdam: North-Holland)
Hirasawa, T. 1969, Prog. Theor. Phys., 42, 3, 523
Hollenbach, D., & McKee, C. F. 1979, ApJS, 41, 555
Hutchins, J. B. 1976, ApJ, 205, 103
Jeans, J. H. 1928, Astronomy and Cosmogony (Cambridge: Cambridge Univ Press)
Karpas, Z., Anicich, V., & Huntress, W. T. 1979, J. Chem. Phys., 70, 2877
Kashlinsky, A., & Rees, M. J. 1983, MNRAS, 205, 955
Kolb, E. W., & Turner, M. S. 1990, The Early Universe (Redwood City: Addison-Wesley)

Lahav, O. 1986, MNRAS, 220, 259
Larson, R. B. 1969, MNRAS, 145, 271
Lepp, S., & Shull, J. M. 1983, ApJ, 270, 578
———. 1984, ApJ, 280, 465
Mather, J. C., et al. 1994, ApJ, 420, 439
Matsuda, T., Sato, H., & Takeda, H. 1969, Prog. Theor. Phys., 42, 2, 219
Nakashima, K., Takayi, H., & Nakamura, H. 1987, J. Chem. Phys., 86, 726
Navarro, J. F., & White, S. D. M. 1994, MNRAS, 267, 401
Osterbrock, D. E. 1974, Astrophysics of Gaseous Nebulae (San Francisco: Freeman)
Palla, F., Salpeter, E. E., & Stahler, S. W. 1983, ApJ, 271, 632
Press, W. H., & Gunn, J. E. 1973, ApJ, 185, 397
Press, W. H., Teukolsky, S. A., Vetterling, W. T., & Flannery, B. P. 1992, Numerical Recipes in Fortran (2d ed.; Cambridge: Cambridge Univ. Press)
Peebles, P. J. E. 1993, Principles of Physical Cosmology (Princeton: Princeton Univ. Press), 179, 635
Peebles, P. J. E., & Dicke, R. H. 1968, ApJ, 154, 891
Quinn, T., Katz, N., & Efstathiou, G. 1995, MNRAS, submitted
Rawlings, J. M. C. 1988, MNRAS, 232, 507
Rawlings, J. M. C., Drew, J. E., & Barlow, M. J. 1993, MNRAS, 265, 968
Richstone, D., Loeb, A., & Turner, E. L. 1992, ApJ, 393, 477
Ruzmaikina, T. V. 1973, Soviet Astron., 16, 6, 991
Saslaw, W. C., & Zipoy, D. 1967, Nature, 216, 976
Shapiro, P. R., Giroux, M. L., & Babul, A. 1994, ApJ, 427, 25
Shapiro, P. R., & Kang, H. 1987, ApJ, 318, 32
Silk, J. 1983, MNRAS, 205, 705
Spitzer, L. Jr., & Hart, M. H. 1971, ApJ, 166, 483
Stancil, P. C. 1994, ApJ, 430, 360
Steinmetz, M., & Muller, E. 1994, A&A, 281, L97
Thoul, A. A., & Weinberg, D. H. 1995, ApJ, 442, 480
Tytler, D., & Fan, X. M. 1995, ApJ, in press
White, M., Scott, D., & Silk, J. 1994, ARA&A, 32, 319
White, S. D. M. 1994, Les Houches Lectures (Amsterdam: Elsevier) in press